Control of a gas-liquid inline swirl separator based on tomographic measurements

Garcia, M. M.; Sahovic, B.; Sattar, M. A.; Atmani, H.; Schleicher, E.; Hampel, U.; Babout, L.; Legendre, D.; Portela, L. M.

DOI
10.1016/j.ifacol.2020.12.588

Publication date
2020

Document Version
Final published version

Published in
IFAC-PapersOnline

Available online at www.sciencedirect.com

ScienceDirect

IFAC Papers Online CONFERENCE PAPER ARCHIVE

IFAC PapersOnLine 53-2 (2020) 11483–11490

Control of a Gas-Liquid Inline Swirl Separator Based on Tomographic Measurements

M.M. Garcia * **B. Sahovic** ** **M. A. Sattar** *** **H. Atmani** ****
E. Schleicher ** **U. Hampel** ** **L. Babout** *** **D. Legendre** ****
L.M. Portela *

* *Department of Chemical Engineering, Delft University of Technology, Delft, Netherlands (e-mail: m.martinezgarcia@tudelft.nl, l.portela@tudelft.nl)*

** *Institute of Fluid Dynamics, Helmholtz-Zentrum Dresden – Rossendorf, Dresden, Germany (e-mail: b.sahovic@hzdr.de, e.schleicher@hzdr.de, u.hampel@hzdr.de*

*** *Institute of Applied Computer Science, Lodz University of Technology, Lodz, Poland (e-mail: muhammad.sattar@p.lodz.pl, laurent.babout@p.lodz.pl)*

**** *Institut de Mécanique des Fluides de Toulouse, Université de Toulouse, Toulouse, France (e-mail: hanane.atmani@imft.fr, dominique.legendre@imft.fr)*

Abstract: This text structures the application of Wire-Mesh sensors and Electrical Resistance Tomography in the control of an Inline Swirl Separator. It introduces a mechanistic model of the two-phase flow inside the device, which is linearized around an ideal perfect operation, and implemented in a Model Predictive Controller. The whole text is structured aiming at a future real application of the controller, briefly introducing the setup that is going to be used, the sensors and their working principles. The results obtained show a stable controller, able to regulate the process relatively fast in relation to the time resolution of the sensors. The positive response of the approach stimulates further improvements in the model developed, and the implementation of more sophisticated techniques to handle the non-linearities of the process.

Keywords: Cyclone, Swirl Separator, Gas-Liquid Flow, Tomography, Model Based Control, Process Control

1. INTRODUCTION

Petroleum is not found pure in nature. The substance is commonly extracted from the oil wells together with water, gas and sand. Among the techniques that can be applied to isolate oil from the remaining components, the use of cyclones (or swirl separators) has bought some attention along the years due to the ability of the device of separating fluids at high flow rates, its efficiency in handling small particles, and its compactness.

Cyclones rely on centripetal forces to separate the incoming mixture. A very strong swirl motion is created inside the device, leading to accelerations of $\sim O(100g)$. Although this huge acceleration is fundamental to the separation process, it brings a complex flow behavior, that is highly turbulent and presents continuous oscillations in the distribution of phases (fluids) inside the equipment. Moreover, the conditions in an oil field are not constant over time, with changes in the operational conditions of the equipment. One example would be the passage of a gas burst through the device, a situation where the gas amount crossing the separator increases a lot in relation to the average operational value.

The recent progresses on tomography and computation now allow the "real-time" monitoring of the separation process, which opens the door to a real time control of cyclones. As the physics behind the separation process is relatively known, this knowledge can be used to build "smart" controllers that do not rely on pure feedback action, but are able to predict the mixture behavior inside the separator in advance and start acting on the flow before it leaves the device. In such a context, Model Predictive Control (MPC) was chosen to regulate the process based on disturbances measured at locations upstream the separation. Naturally, the approach comes with the cost of developing a model that predicts the separation based on measurements far from the location.

This text introduces a flow model and its virtual implementation in a MPC controller, although the whole structure is based on a future real application. It starts describing the setup and sensors that are going to be used in the project (Sec. 2). The topic is followed by a brief introduction to the Computational Fluid Dynamics (CFD) simulations being carried out to obtain a deeper understanding of the physics of the separation process (Sec. 3), and to improve the flow model described in Sec.

10.1016/j.ifacol.2020.12.588

4 present inside the controller. Section 5 is concerned with the development and implementation of a (multiple) MPC controller. The results of the approach are briefly explored in Sec. 6.

2. EXPERIMENTAL FACILITY

2.1 Swirl Flow Separator

The separator considered in this project consists of a scaled-down version of the device developed by van Campen (2014) for oil-water flows. A PI control of the original device was present two years ago in this same conference, by Das and Jäschke (2018). As the main focus of the current work is to study the possibility of controlling an inline swirl separator based on tomographic measurements, the fluids were changed to an air-water mixture, that is easier to handle and does not lead to the emulsions sometimes generated in oil-water flows.

The separator is composed by a vaned element (the swirl element), that generates the swirling flow, the swirl tube, where the separation takes place, and two outlets, each one capturing the majority of one of the fluids (or phases). A sketch of the separator is presented in Fig. 1.

The intensity of the swirl motion is defined by the geometry of the swirl element. If properly sized, the swirl motion inside the separator generates a core of the lighter phase, that flows in the central region of the swirl tube, and an annulus of the heavier phase, that flows close to the wall. Here, the lighter phase corresponds to air, and the heavier phase to water.

At the end of the separator, the (majority of the) lighter phase should be captured by the outlet at the center of the pipe, called pickup tube (inner tube or vortex finder), while the (majority of the) heavier phase should captured by the outer tube.

To make sure the fluids are being properly separated, the device is controlled by 2 valves, placed individually at the two outlets of the separator. An ideal separation would have all the lighter phase (air) crossing the pickup tube and all the heavier phase (water) crossing the outer tube.

The monitoring of the process is done by Wire-Mesh Sensors (WMS) and Electrical Resistance Tomography (ERT). A two-layer WMS is placed upstream the separator, providing information about the flow properties of the mixture entering the device. The ERT measures the distribution of phases inside the separator, which, together with the WMS data and a dynamic mechanistic model of the flow, can be propagated through the entire separator. To provide a feedback of the separation, an additional sensor that measures the fraction of each fluid is considered at the two outlets of the equipment. The sensor choice is left open in this work; possible options would be extra wire-mesh sensors, additional ERT systems, scales or flow meters, depending on the time resolution desired.

2.2 The wire-mesh sensor

A wire-mesh sensor (Fig. 2) consists of two planes of parallel wires placed in a pipe cross-section (Prasser et al., 1998). They are separated by a small axial distance, with

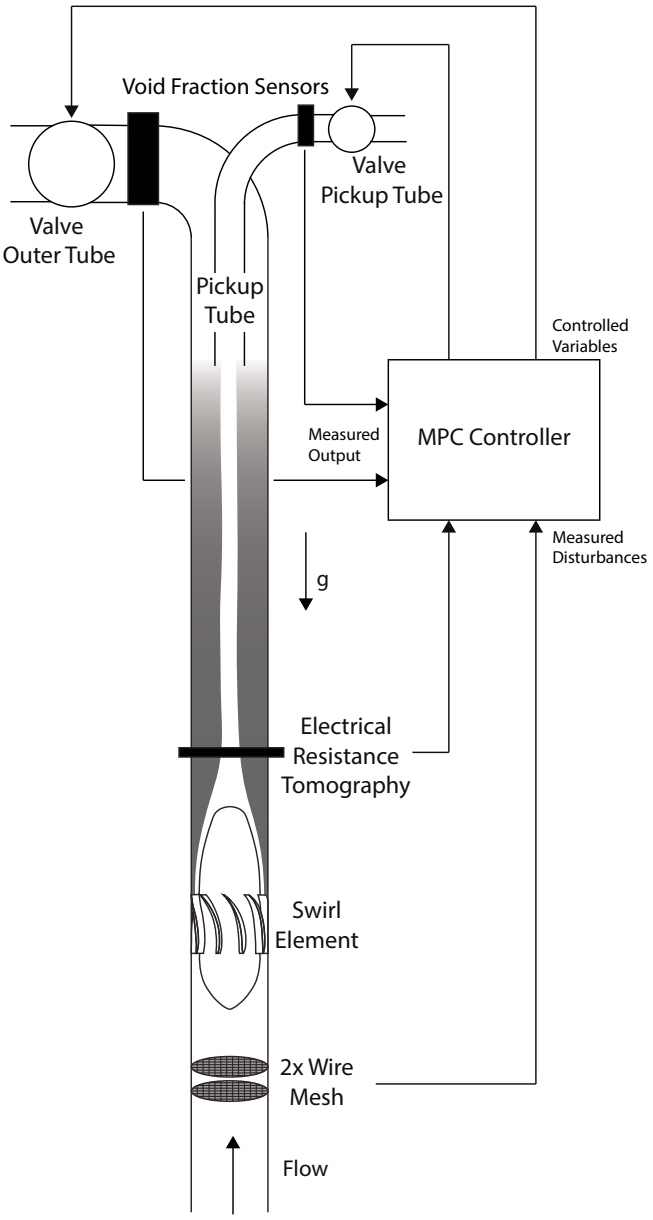

Fig. 1. Schematics of the Swirl Separator with the sensors and valves considered in the project. Gray represents the heavier phase (water) and white represents the lighter phase (air) inside the separator.

the wires of one plane arranged perpendicularly to the wires of the other plane, forming a number of virtual wire crossings. In one plane (transmitter), wires are sequentially activated with a voltage while, at the other plane, the transmitted electrical currents are simultaneously sampled by the (receiver) wires. The technique is able to measure the electrical conductance values in each single crossing-points with a sampling rate of up to 10,000 frames per second. Details about the WMS being used, and some results already obtained by it, can be found in Sahovic et al. (2018).

Volumetric Fraction Measurement: In a first approximation, the local instantaneous measured conductance in a single crossing point is assumed to be linear related with the local liquid holdup. Thus, the local instantaneous void

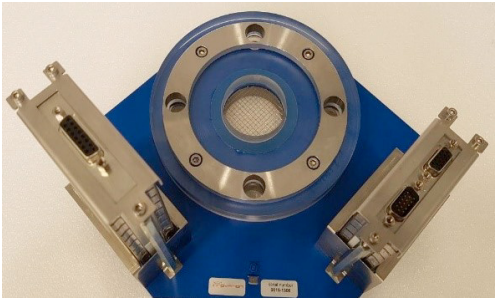

Fig. 2. Wire-mesh sensor to be installed in the flow loop.

fraction $\varepsilon(i,j,k)$ in a single crossing point (i,j) and sample number k is derived by:

$$\varepsilon(i,j,k) = 1 - \frac{U^{meas}(i,j,k)}{U^{W}(i,j)} \tag{1}$$

where $U^{meas}(i,j,k)$ denotes the local instantaneous sensor signal of the measured value and $U^{W}(i,j)$ the time averaged sensor signal of a full liquid calibration measurement.

To get the averaged void fraction across the entire sensor for each frame, a spatial averaging of the single void fraction values is done. The average is calculated considering weighting coefficients $a(i,j)$ to damp the contribution of the virtual dots close to the pipe wall. The cross-sectional averaged void fraction $\overline{\varepsilon}_k$ can be calculated for each sampling period k individually by:

$$\alpha^{WMS}(t) = \overline{\varepsilon}_k = \sum_i \sum_j a(i,j)\varepsilon(i,j,k) \tag{2}$$

The result of the data evaluation is a sequence of instantaneous cross sectional averaged volumetric gas fractions for each frame at the wire-mesh location.

Interfacial Area Velocity Measurement: A velocity profile can be obtained from a pair of wire mesh sensors mounted adjacent in a flow loop. To do this, the signals from both measurement planes are cross-correlated separately for each pair of mesh points, which are located above each other. In the case of axisymmetric flows (e.g. vertical pipes), the obtained cross-correlation can be averaged in circumferential direction using the same weight coefficients of the void fraction measurement. As a result, the average interfacial area velocity as a function of r is calculated from the corresponding time-shift:

$$U_g^{WMS}(r) = \frac{\Delta L_{1-2}}{\Delta k_{max}} f_{meas} \tag{3}$$

with Δk_{max} corresponding to highest detection of averaged cross correlation, and ΔL_{1-2} corresponding to the distance between the two WMS. For bubbly flows, the calculated Interfacial area velocity can be interpreted as the gas velocity at the sensor location.

2.3 The Electrical Resistance Tomography Sensor

The Electrical Resistance Tomography (ERT) sensor is used to visualize the gas core inside the separator. The technique has been widely explored in the last few decades due to its high measurement speed, low implementation cost, and straightforward implementation (Ren et al., 2017).

Although non-intrusive, ERT based sensors require contact with the medium under observation, so the current can flow through the media. A typical ERT system consists of three parts: (i) Data acquisition hardware, (ii) a sensor and (iii) image visualization and reconstruction software (Stanley and Bolton, 2008).

The approach chosen for the project is based on the voltage injection and current measurement (VC) scheme. The principle of VC scheme is that one electrode acts as a source electrode, and all of the other electrodes, (excluding the source electrode) acts as sink electrodes (Kim et al., 2014). The VC scheme of measurement is shown in Fig 3a. Any change in the investigated media causes a perturbation of the electric field, which results in measured current fluctuations between pairs of electrodes, as illustrated in Fig 3b.

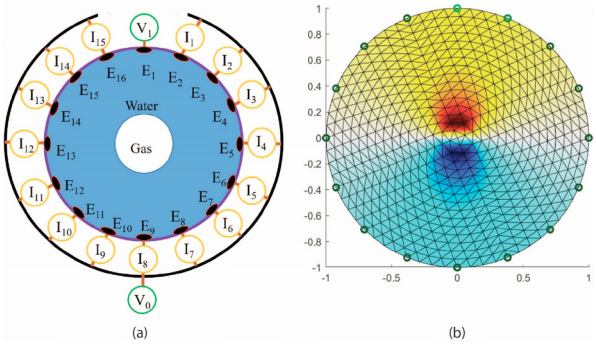

Fig. 3. Measurement Principle of the ERT system. (a) VC protocol. (b) Influence in the current by the electric field distribution.

An image of the media can be retrieved from the set of current measurements. The gas core information is extracted from the reconstructed void fraction distribution via the geodesic active contour (GAC) technique. Fig 4b presents the plot of the equivalent gas core radius, obtained via the GAC image processing, on the top of a ERT reconstructed image.

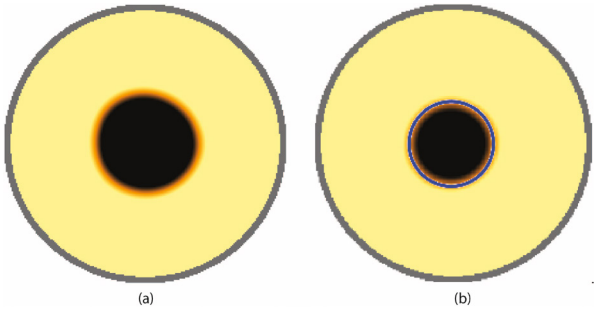

Fig. 4. Gas core imaging.(a) Image obtained via the Dynamical Bayesian image reconstruction.

The sensor designed for the project consists of 16 stainless steel electrodes of circular shape, placed equidistantly around the pipe. During tests, the sensor was able to generate a data acquisition frame rate of 16Hz, with a frequency of live reconstruction of 4Hz.

3. COMPUTATIONAL FLUID DYNAMICS

Computational Fluid Dynamics (CFD) simulations are adopted to support the investigation of the physics behind the separation process, allowing improvements in the mechanistic model proposed in this text.

In the simulations, Immersed Boundary Method (IBM) (Bigot et al., 2014) is used to simulate the pipe, the swirl element and the pick-up tube. The bubbles are tracked using Lagrangian tracking (Chouippe et al., 2014) and a switch to Volume of Fluid (VoF) (Abadie et al., 2015) is done to simulate the gas core after the swirl element. The approach results in extra source terms (volumetric forces) in the Navier-Stokes (NS) equations, describing the contributions of the IBM, VoF and Lagrangian Tracking techniques. The numerical simulations are done using the in-house code JADIM. Figure 5 illustrates a result obtained by a CDFD simulation.

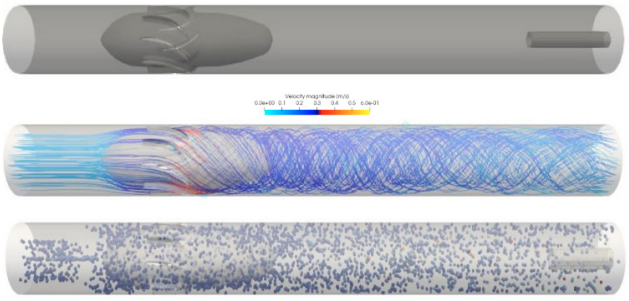

Fig. 5. Top: Geometry of the inline separator as used in the IBM simulation. Middle: Streamlines of single-phase flow for Re=4600. Bottom: Two-phase flow simulation using the coupling of Immersed Boundary Method and Lagrangian Tracking.

4. A SIMPLIFIED MODEL OF THE FLOW

The conservation of mass and the Navier-Stokes equations solved by CFD techniques have to be considerably simplified to be computed fast enough by the controller. In this article, integral balances are used to simplify the equations based on: (i) the hypothesis axisymmetry, (ii) an analysis of the order of magnitude of the terms contained in the equations and (iii) the integral of the equations in the radial direction inside each phase (air or water). The approach leads to the integral balances described below, in which the phases are denoted by the subscript "j". In the equations, z corresponds to the axial direction inside the separator, ρ_j the density of the phase "j", u_z and u_θ the velocity components in the axial and azimuthal directions, p the pressure and τ_{ab} the components of the shear stress tensor. In the remaining of the report, $j = 1$ is used to indicate the lighter phase (air), and 2 the heavier phase (water) inside the device.

$$\frac{\partial}{\partial t}\int_j \rho r dr + \frac{\partial}{\partial z}\int_j \rho u_z r dr = 0 \tag{4}$$

$$\int_j \frac{\partial p}{\partial r} dr = \int_j \frac{\rho u_\theta^2}{r} dr \tag{5}$$

$$\frac{\partial}{\partial t}\int_j \rho u_\theta r^2 dr + \frac{\partial}{\partial z}\int_j \rho u_z u_\theta r^2 dr = \int_j \frac{\partial r^2 \tau_{r\theta}}{\partial r} dr \tag{6}$$

$$\begin{aligned}\frac{\partial}{\partial t}\int_j \rho u_z r dr + \frac{\partial}{\partial z}\int_j \rho u_z^2 r dr = \\ -\int_j \frac{\partial (p+\rho g z) r}{\partial z} dr + \int_j \frac{\partial r \tau_{rz}}{\partial r} dr\end{aligned} \tag{7}$$

4.1 Flow Profiles

The integrals in the radial direction require some approximation of the velocity profiles to be evaluated. The azimuthal velocity in bounded single-phase swirling flows present a self-similar profile, described by (i) a solid body rotation close to the center of the pipe, (ii) a transition region and (iii) a decaying velocity region close to the wall (Kitoh, 1991; Chang and Dhir, 1994).

Based on the single-phase distributions mentioned, the current model assumes that the gas core, due to its central location, can be approximated as presenting a solid body rotation: $u_{1,\theta}(r,z) = \omega_1(z) r$. The liquid, on the other hand, accumulates close to the wall and is approximated as presenting a constant circulation: $u_{2,\theta}(r,z) = \Gamma_2(z)/(2\pi r)$. The azimuthal velocity does not necessarily match at the interface, as ω_1 and Γ_2 are considered as independent variables in the context problem.

As a simplification of notation in the upcoming equations, indicatives of the azimuthal velocity are defined as:

$$\begin{aligned} v_1 &= \omega_1 \alpha R \\ v_2 &= \Gamma_2/(2\pi R) \end{aligned} \tag{8}$$

where α is the volumetric fraction of gas (void fraction) in a cross section of the separator, and is related to the interface position by $\alpha = R_i^2/R^2$; R corresponds to the radius of the device and R_i is the (local) radial position of the interface.

Due to the lack of knowledge about the axial velocity profiles, that present significant changes from case to case even in single phase flows, uniform values are assumed for each phase, i.e., $u_{1,z} = u_1(z)$ and $u_{2,z} = u_2(z)$.

Applying the azimuthal velocity profiles on (5) leads to a radial pressure distribution described by:

$$p(r,z) = \begin{cases} p_i + \rho_1 \dfrac{v_1^2}{2}\dfrac{1}{\alpha^2}\left(\dfrac{r^2}{R^2} - \alpha\right) & \text{if } r \le R_i \\ p_i + \rho_2 \dfrac{v_2^2}{2}\left(\dfrac{1}{\alpha} - \dfrac{R^2}{r^2}\right) & \text{if } r > R_i \end{cases} \tag{9}$$

in which the pressure was assumed the same at both sides of the interface (no surface tension effects were considered), and represented by p_i in the equation.

4.2 Integral Balances

Considering the axial and azimuthal velocity profiles mentioned, and assuming that the gas phase presents a constant density, the integral balances of (4)-(7) lead to:

$$\frac{\partial \alpha}{\partial t} + \frac{\partial \alpha u_1}{\partial z} = 0 \tag{10}$$

$$\frac{\partial (1-\alpha)}{\partial t} + \frac{\partial (1-\alpha) u_2}{\partial z} = 0 \tag{11}$$

$$\frac{\partial v_1}{\partial t} + u_1 \frac{\partial v_1}{\partial z} = \frac{4}{\rho_1 R} \tau_{r\theta\, i} \tag{12}$$

$$\frac{\partial v_2}{\partial t} + u_2 \frac{\partial v_2}{\partial z} = \frac{2}{\rho_2 R} \frac{1}{1-\alpha} \left(\tau_{r\theta\, w} - \alpha \tau_{r\theta\, i} \right) \tag{13}$$

$$\begin{aligned} \rho_1 \frac{\partial \alpha u_1}{\partial t} + \rho_1 \frac{\partial \alpha u_1^2}{\partial z} = -\alpha \frac{\partial p_i}{\partial z} + \rho_1 \frac{\partial}{\partial z} \left(\frac{v_1^2}{4} \right) \\ -\rho_1 \alpha g + \frac{2\sqrt{\alpha}}{R} \tau_{rz\, i} \end{aligned} \tag{14}$$

$$\begin{aligned} \rho_2 \frac{\partial (1-\alpha) u_2}{\partial t} + \rho_2 \frac{\partial (1-\alpha) u_2^2}{\partial z} = -(1-\alpha) \frac{\partial p_i}{\partial z} \\ -\rho_2 \frac{\partial}{\partial z} \left[\frac{v_2^2}{2} \left(\frac{1-\alpha}{\alpha} + \ln \alpha \right) \right] - \rho_2 (1-\alpha) g \\ + \frac{2}{R} \left(\tau_{rz\, w} - \sqrt{\alpha} \tau_{rz\, i} \right) \end{aligned} \tag{15}$$

where the subscript "i" describes interface values ($\tau_{rz\, i}$ is the shear stress acting in the axial direction at the interface), and the subscript "w" is used to describe wall quantities.

The mass equations - (10) and (11) - share the same time derivative, and can be combined into the spatial conservation of mixture velocity, defined as:

$$u_m \equiv \alpha u_1 + (1-\alpha) u_2 \tag{16}$$

After some manipulation of the linear momentum equations - (14) and (15) - the p_i term can be eliminated, and the equations combined into:

$$\begin{aligned} \frac{\rho_1}{\rho_2} \frac{\partial u_1}{\partial t} - \frac{\partial u_2}{\partial t} = -\frac{\rho_1}{\rho_2} \frac{\partial}{\partial z} \left(\frac{u_1^2}{2} \right) + \frac{\rho_1}{\rho_2} \frac{1}{\alpha} \frac{\partial}{\partial z} \left(\frac{v_1^2}{4} \right) \\ + \frac{\partial}{\partial z} \left(\frac{u_2^2}{2} \right) + \frac{1}{1-\alpha} \frac{\partial}{\partial z} \left[\frac{v_2^2}{2} \left(\frac{1-\alpha}{\alpha} + \ln \alpha \right) \right] \\ + \left(1 - \frac{\rho_1}{\rho_2} \right) g + \frac{2}{\rho_2 R} \frac{1}{1-\alpha} \left(\frac{1}{\sqrt{\alpha}} \tau_{rz\, i} - \tau_{rz\, w} \right) \end{aligned} \tag{17}$$

The current model assumes that the mixture velocity is constant over time, which allows the obtainment of an explicit set of equations by expanding u_2 (including the time derivative) based on (16):

$$\frac{\rho_1}{\rho_2} \frac{\partial u_1}{\partial t} - \frac{\partial u_2}{\partial t} = \left(\frac{\rho_1}{\rho_2} + \frac{\alpha}{1-\alpha} \right) \frac{\partial u_1}{\partial t} + \frac{u_m - u_1}{(1-\alpha)^2} \frac{\partial \alpha u_1}{\partial z} \tag{18}$$

in which the temporal derivative can be easily isolated by sending the space term to the right side of the equation, and diving the resulting expression by the $(\rho_1/\rho_2 + \alpha/(1-\alpha)$ term. If the mixture velocity varies considerably with time, the axial velocities must be left apart, and (16) must be evaluated either as part of an implicit state space model (with zero time derivative for the equation), or via an equality constraint implemented in the controller.

The flow dynamics inside the separator is fully described by: (10), (12), (13) and the explicit version of (17).

4.3 Stress Relations

The stress terms of the equations need some closure relations. As common in multiphase modeling, the axial stresses are approximated by:

$$\tau_{rz\, i} = -f_{z\, i} \rho_1 \frac{(u_1 - u_2)|u_1 - u_2|}{2} \tag{19}$$

$$\tau_{rz\, w} = -0.005 \rho_2 \frac{u_2 |u_2|}{2} \tag{20}$$

and the angular stresses are approximated based on an extension of the single phase study of Kitoh (1991), as:

$$\tau_{r\theta\, i} = -0.005 \frac{1}{\sqrt{\alpha}} \rho_1 \frac{(v_1 - v_2)|u_1 - u_2|}{2} \tag{21}$$

$$\tau_{r\theta\, 2} = -0.01 \frac{1}{1-\alpha} \rho_2 \frac{v_2 |u_2|}{2} \tag{22}$$

Note that the angular stress approximations have no current validation for the multiphase scenario at this point. Future works involve the analysis of the terms.

4.4 Domain Discretization

The set of PDEs describing the flow motion are converted into ODEs via a discretization of the domain inside the separator. This is achieved considering a Finite Volume Method with a centered scheme, i.e., for the cell k inside the domain, the derivative of the property f is approximated by:

$$\frac{\partial f}{\partial z}(k) \approx \frac{f(k+1) - f(k-1)}{2 \Delta z} \tag{23}$$

The approach turns the 4 PDES into a set of $4n$ ODEs, in which n is the total number of cells being modeled inside the flow domain.

4.5 Model Boundary Conditions and Valve Models

Inlet: The ERT, placed right after the swirl element, measures the local gas core area over time. The value is directly applied to a ghost cell of size Δz placed before the element $k = 1$ in the equations describing the flow.

The wire mesh sensor is able to evaluate the air velocity and void fraction upstream the swirl element for some scenarios of upcoming flow pattern (bubbly and plug flows). The velocity measured can be connected to the mixture velocity by slip relations found in the literature. As the fluids are assumed incompressible, the mixture velocity estimated is the same across the entire flow.

For a steady state operation, the combination of ERT and WMS would result in the gas velocity u_1 of the

ghost cell, via the conservation of mass. However, in an unsteady scenario, the mass of gas contained inside the swirl element can change over time, and there is a delay between the changes in the flow observed by the 2 sensors (any change in the gas properties at the WMS must be travel to the ERT to be detected). At this point, instead of attempting to model the delay term or the change in the gas contained inside the swirl element region, it is assumed that the swirl element presents a punctual behavior, i.e., the location suddenly generates the swirl motion, and the signals of the WMS and ERT are connected by the steady state expression. Some tuning of a delay term based on experimental conditions can be achieved in the future.

The angular momentum terms cannot be measured at the ERT location. Then, the values at the ghost cell placed there are estimated based on the conditions measured by the WMS and ERT, and the swirl element geometry. In this article, the angular velocity representatives are obtained by assuming that both phases share the same axial velocity inside the swirl element, and that the azimuthal velocities match at the interface, resulting in the approximations for the ghost cell given by:

$$v_1 = v_2 = 2.7 u_m \tan(\phi) \tag{24}$$

Details on the swirl element geometry that results in the expressions can be found in van Campen (2014); Star (2016). In the expressions, ϕ corresponds to the angle of the vanes of the swirl element.

Outlet: An additional cell is considered representing the pipelines with the valves and void fraction sensors at the outlets. This corresponds to an approximation of the region, as in reality the flow still propagates in the pipelines until it reaches the sensors and valves, so there is a delay between the separation itself and its measurement. Moreover, there is an underestimation of the inertia of the real elements, as the entire fluid contained in each outlet must be accelerated instead of the fluid contained in a small virtual cell.

An schematics of the simplified valve model adopted during this work is presented in Fig. 6.

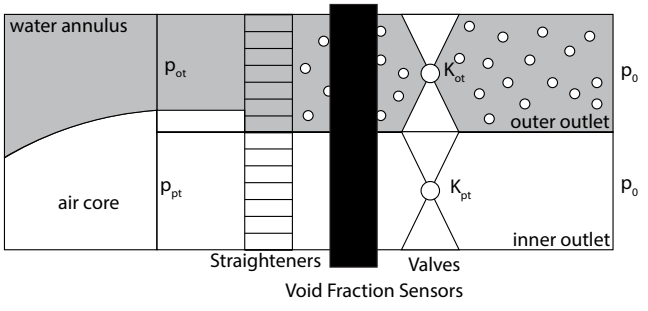

Fig. 6. Approximation of the outlets in the model. The element is adopted as presenting the same size of the cells in the grid representing the flow. The image represents a "thick" core condition, where part of the gas is captured by the outer tube.

It is assumed an homogeneous model of the flow for each outlet, i.e., each outlet presents a single velocity shared by the two phases. As a consequence, since the area is fixed, the balance of mass on each valve results in a constant velocity inside the element, and the balance of linear momentum of each valve results in:

$$\rho_v \frac{du_v}{dt} = \frac{1}{\Delta z}\left(p_{v\,in} - K_v \rho_v \frac{u_v^2}{2} - p_{v\,out}\right) \tag{25}$$

where K_v corresponds to the loss coefficient of the valve. The pressure values at the inlet of the valves (in) and at the outlet of the valves (out) correspond to average values (in the radial direction).

The outlets are assumed sharing the same pressure after the valves, e.g. a separator open to atmosphere or sharing the same tank, and it is assumed that the flow straighteners act dissipating the totality of the angular momentum arriving at the location, without impacting the linear momentum. Then, the linear momentum balance of one valve can be subtracted from the other, resulting in:

$$\rho_{pt}\frac{du_{pt}}{dt} - \rho_{ot}\frac{du_{ot}}{dt} = \frac{1}{\Delta z}\left(p_{pt\,in} - p_{ot\,in} - K_{pt}\rho_{pt}\frac{u_{pt}^2}{2} + K_{ot}\rho_{ot}\frac{u_{ot}^2}{2}\right) \tag{26}$$

where "pt" represents the average flow properties at the pickup tube (inner outlet), and "ot" represents the average flow properties of the outer tube.

As the mixture velocity of the entire system is the same, the u_{ot} term can be replaced in the expressions by $u_{ot} = (u_m - \beta u_{pt})(1-\beta)$, where β represents the ratio between the inner pipe area and the total pipe area. Finally, the time derivative of the inner valve velocity can be written explicitly as:

$$\frac{du_{pt}}{dt} = \left(\rho_{pt} + \frac{\beta}{1-\beta}\rho_{ot}\right)^{-1}\frac{1}{\Delta z}\left(p_{pt\,in} - p_{ot\,in} - K_{pt}\rho_{pt}\frac{u_{pt}^2}{2} + K_{ot}\rho_{ot}\frac{u_{ot}^2}{2}\right) \tag{27}$$

The equivalent density of the flow crossing the outlets is connected to the position of the interface at the entrance of the region, and impacts the efficiency of the valves in regulating the flow. Moreover, the average pressure values of each outlet also depend on the position of the interface, due to the swirl contribution. As consequence, two separated plant models must be considered to properly represent the dynamics of the flow crossing the valve regions. This also impacts the controller, that needs to combine two different routines depending on the position of the interface.

For a "thick" core condition, as illustrated in Fig. 6, the terms of (27) are given by:

$$\begin{aligned}
\rho_{pt} &= \rho_1 \\
\rho_{ot} &= \rho_1 \frac{\alpha_v - \beta}{1-\beta} + \rho_2 \frac{1-\alpha_v}{1-\beta} \\
u_{pt} &= u_{1\,v} \\
u_{ot} &= u_{1\,v} \frac{\alpha_v - \beta}{1-\beta} + u_{2\,v} \frac{1-\alpha_v}{1-\beta} \\
p_{pt\,in} - p_{ot\,in} &= -\rho_1 \frac{v_{1\,v}^2}{4} \left(\frac{2\alpha_v - \alpha_v^2 - \beta}{\alpha_v^2 (1-\beta)} \right) \\
&\quad -\rho_2 \frac{v_{2\,v}^2}{2} \left(\frac{1-\alpha_v}{\alpha_v (1-\beta)} + \frac{1}{1-\beta} \ln(\alpha_v) \right)
\end{aligned} \tag{28}$$

and for a "thin" core condition, i.e., $\alpha_v < \beta$:

$$\begin{aligned}
\rho_{pt} &= \rho_1 \frac{\alpha_v}{\beta} + \rho_2 \frac{\beta - \alpha_v}{\beta} \\
\rho_{ot} &= \rho_2 \\
u_{pt} &= u_{1\,v} \frac{\alpha_v}{\beta} + u_{2\,v} \frac{\beta - \alpha_v}{\beta} \\
u_{ot} &= u_{2\,v} \\
p_{pt\,in} - p_{ot\,in} &= -\rho_1 \frac{v_{1\,v}^2}{4\beta} - \rho_2 \frac{v_{2\,v}^2}{2} \left(\frac{1}{\beta} + \frac{\ln \beta}{1-\beta} - \ln \left(\frac{\alpha_v}{\beta} \right) \right)
\end{aligned} \tag{29}$$

which are replaced in the expression for the respective "thick" and "thin" versions of the plant. Note that for the thin core condition, the du_{pt}/dt term results in time derivatives of both u_1 and α. The α derivative can be eliminated from the equation by replacing the gas mass balance of the location, as done in the previous linear momentum manipulation. The remaining balances of the valve element are modeled via an upward discretization (i.e., the spatial derivatives are approximated based on the quantities at the last cell of the flow and the outlet values itself). Both valve models result in the same expression for the perfect separation condition, when $\alpha_v = \beta$.

4.6 Linearization and Steady State Simplification

The flow equations are linearized around the condition of perfect separation ($\alpha_v = \beta$).

As a simplification, a steady state distribution of gas described by a third degree polynomial is assumed instead of modeling the remaining stress term ($f_{z\,i}$) of the equations. The polynomial is chosen to have a zero gradient on both the entrance and exit of the domain. The choice is based on the fact that far from the valves the flow does not feel the presence of the elements, and that the flow no longer changes its distribution after reaching the outlets.

Then, the steady state void fraction distribution is approximated by:

$$\alpha(z) = \left(\beta - \alpha^{ERT}\right) p(z) + \alpha^{ERT} \tag{30}$$

where

$$p(z) = \begin{cases} 0 & \text{for } z \le z_0 \\ -2 \left(\dfrac{z - z_0}{L - z_0} \right)^3 + 3 \left(\dfrac{z - z_0}{L - z_0} \right)^2 & \text{for } z > z_0 \end{cases} \tag{31}$$

z_0 is a constant indicating the beginning of the region affected by the valves in relation to the swirl element.

This distribution chosen for the steady state profile is not natural, and is used to close the equations of the problem while realistic correlations for the stress factors are not explored. Ideally, all the stress terms would be modeled via experimental correlations, and the steady state distribution would be recovered from the non-linear set of equations involving those terms.

The area approximation allows (i) the calculation of the axial velocity distributions via (10) and (16), (ii) the propagation of the angular velocity terms in an upward manner via (12) and (13), and the use of the centered form of (17) to recover the distribution of $f_{z\,i}$ for the cells distributed along the separator. Any of the two valve conditions can be used to provide a relation between the inner valve and outer valve coefficients when solving the perfect separation problem. The inner valve is set to $K_{pt} = 1$ to close the set of steady-state variables.

Now, the Jacobian of the expressions can be calculated to linearize the plant around the steady state distribution assumed, and the state-space representations of the system can be built. From this part of the report on, the variables presented in the MPC model equations are no longer the flow values, but small fluctuations around the steady state distribution assumed, due to the linearization step.

5. MPC MODEL

The vector of states is built as:

$$\begin{aligned}
x = [&\alpha(k=1) \cdots \alpha(k=n) \quad \alpha_v \quad u_1(1) \cdots u_1(n) \quad u_{1\,v} \\
&v_1(1) \cdots v_1(n) \quad v_{1\,v} \quad v_2(1) \cdots v_2(n) \quad v_{2\,v}]^T
\end{aligned} \tag{32}$$

where k represents the cell in the grid and v represents the inner tube values. The boundary conditions of the problem are given by the sensors, thus being considered as measured disturbances: $\nu = \begin{bmatrix} \alpha^{ERT} & u_1^{ERT} \end{bmatrix}^T$.

The manipulated variables correspond to the 2 valve coefficients, $u = [K_{pt} \quad K_{ot}]^T$. The system presents a single output, given by the void fraction at the outlets: $y = \alpha_v$.

No unmeasured disturbances or inequality constraints were considered in the approach so far, as they required some tests in the real loop to be defined. A possible example would be the study of the operational limits of the control valves, and their effective ranges of loss coefficient.

The cost function optimized by the controller at this point is exclusively based on how far the void fraction fluctuations are from the perfect separation conditions ($J(k) = \sum_{j=N_m}^{N} \hat{y}(k+j|k)^2$). In the future, the rate of changing the valves can be important, e.g. if the separation is considerably disturbed by quick changes in the valves.

The two MPC controllers share the same structure, just differing in the equation for the valve dynamics. They are implemented and tested in Simulink and MATLAB using the "Multiple MPC box", which automatically switches between the 2 MPC models based on the current value of α_v measured at the outlets. The discretization in time of

the equations considers a sampling time of 0.2s, which is close to the current reconstruction time of the ERT. The controller runs parallel to the continuous-time models of the flow in the simulations.

6. RESULTS

The system response to a step fluctuation of 0.1 at $t = 1$ in the void fraction value is presented in Fig. 7. The simulation considered 30 elements in the mesh, a prediction horizon of 5 samples and a control horizon of 2 samples. During the linearization, it was assumed $z_0 = 0$, $\alpha^{ERT} = 0.3$, $u_1^{ERT} = 2$m/s and $u_m = 1$m/s. The separator was considered with 1m length, 10cm diameter, $\beta = 0.25$ and $\phi = 40.2^o$.

The response of this system is clearly marked by a delay of around 0.2s between the change in the ERT value and its detection at the outlets, due to the fact that the enlargement of the core takes time to propagate inside the cyclone. It is notable that the core is adjusted back to very close to the ideal separation condition less than 1s (5 sampling times) after the disturbance is detected by the ERT sensor.

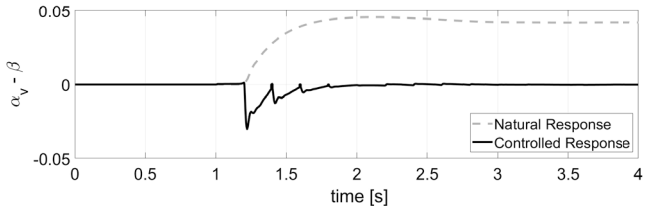

Fig. 7. Model Response to a step change in the ERT void fraction. In dashed line (gray): natural response of the system. In solid line (black): controlled response.

The inputs of the controller are presented in Fig. 8. It shows that the major valve changed to regulate the separation is the outer valve. The result is expected, as the high density of the region turns the pressure difference between the outlets much more sensible to a change in the outer valve coefficient than to a change in the inner one. It is also notable that the MPC starts adjusting the valves before the disturbance reaches the outlets, although the most significant adjusts start after it. The result presents a reduction in the inner valve coefficient of about 0.4 (in relation to the value 1 at steady state), and a maximum increase of 17.3 in the outer valve coefficient, almost twice the steady state value of 19.

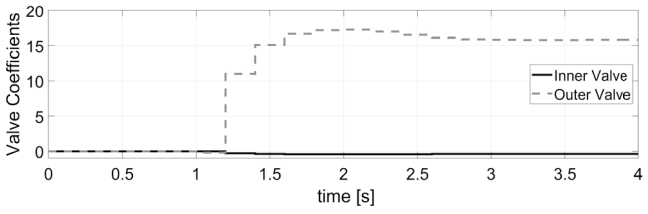

Fig. 8. Change in the Manipulated Variables made by the controller to adjust the flow. In dashed line (gray): Outer Valve coefficient. In solid line (black): Inner valve coefficient.

ACKNOWLEDGEMENTS

This project has received funding from the European Union's Horizon 2020 research and innovation programme under the Marie Skłodowska-Curie grant agreement No 764902 .

The authors acknowledge all the companies and universities involved in TOMOCON, in special to the partners involved in the Swirl Separator topic. They are: G. Lecrivain (Helmholtz-Zentrum Dresden – Rossendorf), M.J. da Silva (Universidade Tecnológica Federal do Paraná), R. Laborde (CERG Fluides S.A.S.), J. Bos (Frames Group B.V.), P. Veenstra (Shell Global Solutions B.V.) and M. Trepte (Teletronic Rossendorf GmbH).

REFERENCES

Abadie, T., Aubin, J., and Legendre, D. (2015). On the combined effects of surface tension force calculation and interface advection on spurious currents within volume of fluid and level set frameworks. *Journal of Computational Physics*.

Bigot, B., Bonometti, T., Thual, O., and Lacaze, L. (2014). A simple immersed boundary method for solid fluid interaction in constant and stratified density flows. *J. Computers and fluids*.

Chang, F. and Dhir, V. (1994). Turbulent flow field in tangentially injected swirl flows in tubes. *International Journal of Heat and Fluid Flow*.

Chouippe, A., Climent, E., Legendre, D., and Gabillet, C. (2014). Numerical simulation of bubble dispersion in turbulent taylor-couette flow. *Physics of Fluids*.

Das, T. and Jäschke, J. (2018). Modeling and control of an inline deoiling hydrocyclone. *IFAC-PapersOnLine*.

Kim, B.S., Khambampati, A.K., Jang, Y.J., Kim, K.Y., and Kim, S. (2014). Image reconstruction using voltage–current system in electrical impedance tomography. *Nuclear Engineering and Design*.

Kitoh, O. (1991). Experimental study of turbulent swirling flow in a straight pipe. *Journal of Fluid Mechanics*.

Prasser, H.M., Böttger, A., and Zschau, J. (1998). A new electrode-mesh tomograph for gas–liquid flows. *Flow measurement and instrumentation*.

Ren, Z., Kowalski, A., and Rodgers, T. (2017). Measuring inline velocity profile of shampoo by electrical resistance tomography (ert). *Flow Measurement and Instrumentation*.

Sahovic, B., Atmani, H., Wiedemann, P., Schleicher, E., Legendre, D., Climent, E., Zamanski, R., Pedrono, A., and Hampel, U. (2018). Investigation of upstream and downstream flow conditions in a swirling inline fluid separator – experiments with a wire-mesh sensor and cfd studies. *9th World Congress on Industrial Process Tomography*.

Stanley, S.J. and Bolton, G.T. (2008). A review of recent electrical resistance tomography (ert) applications for wet particulate processing. *Particle & Particle Systems Characterization*.

Star, S.K. (2016). *Pressure distribution in a liquid-liquid cyclone separator*. Master's thesis, Delft University of Technology.

van Campen, L. (2014). *Bulk dynamics of droplets in liquid-liquid axial cyclones*. Ph.D. thesis, Delft University of Technology.